HAL open science

Influence of 3D-printing on the behaviour of Ti6Al4V in high-speed friction

Mathieu Marquer, Pascal Laheurte, Laurent Faure, Sylvain Philippon

To cite this version:

Mathieu Marquer, Pascal Laheurte, Laurent Faure, Sylvain Philippon. Influence of 3D-printing on the behaviour of Ti6Al4V in high-speed friction. Tribology International, 2020, 152, pp.106557. 10.1016/j.triboint.2020.106557 . hal-03014463

HAL Id: hal-03014463

https://hal.science/hal-03014463v1

Submitted on 22 Aug 2022

HAL is a multi-disciplinary open access archive for the deposit and dissemination of scientific research documents, whether they are published or not. The documents may come from teaching and research institutions in France or abroad, or from public or private research centers.

L'archive ouverte pluridisciplinaire **HAL**, est destinée au dépôt et à la diffusion de documents scientifiques de niveau recherche, publiés ou non, émanant des établissements d'enseignement et de recherche français ou étrangers, des laboratoires publics ou privés.

Distributed under a Creative Commons Attribution - NonCommercial 4.0 International License

Version of Record: https://www.sciencedirect.com/science/article/pii/S0301679X20303881
Manuscript_d933873c2054acd23bf448fd0e8cf3a5

Influence of 3D-printing on the behavior of Ti6Al4V in high-speed friction

Mathieu Marquer[a,*], Pascal Laheurte[a], Laurent Faure[a] and Sylvain Philippon[b]

[a]Université de Lorraine, CNRS, Arts et Métiers ParisTech, LEM3, F-57000 Metz, France
[b]Université de Lorraine, CNRS, ENIM, LEM3, F-57000 Metz, France

ARTICLE INFO

Keywords:
High-speed
Dry friction
Metal
Powder

ABSTRACT

Additive manufacturing techniques, such as Selective Laser Melting (SLM) are considered for making some Ti6Al4V parts. However, in some assemblies, such parts may be subjected to severe sliding.

A Ti6Al4V tribopair was subjected to sliding under high speed and pressure (40 m/s and up to 300 MPa). This research focuses on the influence of the manufacturing process (machining or SLM) and the building orientation (for SLM) of one tribopair element on the friction coefficient and wear.

Results were mostly insensitive to SLM orientation. However, with the SLM parts, there was a higher friction coefficient and a lower wear than with machined parts. An energy-based approach revealed a single pattern for wear regardless of the manufacturing technology, consistent with previous results.

1. Introduction

Titanium, notably in the form of Ti6Al4V alloy, is used for a wide variety of applications. In mechanical engineering, its high specific properties are especially interesting in weight and/or inertia-sensitive applications such as in jet engines [1, 2]. However, titanium alloys behave poorly under tribological solicitations [3] which led to the design of specific coatings, used for example at the blade root/disc slot contact.

Blade/disc assemblies are sometimes subject to severe tribological loadings such as during a bird/ice ingestion event. In these conditions, under up to 400 MPa of contact pressure, a sliding speed of 40 m/s may be reached for a few millimetres. Some studies have looked into the behaviour of such contacts. Chassaing *et al.* [4, 5] considered a worst case scenario where the protective coating had worn off while Marquer *et al.* [6, 7] examined the behaviour of the contact with the coating present. The friction coefficient and wear were shown to be highly dependent on the apparent contact pressure, and less so on the sliding speed (in the high-speed range of their studies). The behaviour of such contacts have also be shown to be relatively independent from the initial roughness of the parts above a critical sliding speed (e.g. 1 m/s for a steel-on-steel contact) [8].

New additive manufacturing processes such as SLM can allow overcoming the limitation of subtractive manufacturing processes (e.g. machining) to optimize the shape of a part and better match form and function [9, 10]. In order to simplify the design, certification, and deployment of parts made by additive manufacturing, the differences and similarities between the behaviour of materials produced by subtractive and additive manufacturing must be known.

Parts obtained by additive and subtractive manufacturing do have distinct properties due to the inherent differences between both kinds of processes. Some of the mechanical properties of SLM-parts can vary markedly from machined ones. For example, Liu *et al.* explain that "the presence of α' martensite in [...] SLM Ti6Al4V significantly increases the ultimate tensile and yield strength by 100-200 MPa but decreases the ductility of the as-built components" [11].

The properties of parts made by additive manufacturing (SLM or other) can be very sensitive to their orientation on the printing bed table. This is especially true for elongated parts, which undergo very different cooling rates depending on their orientation [12, 11, 13, 14]. Furthermore, Ti6Al4V tends to have an anisotropic microstructure and therefore anisotropic mechanical properties [11, 13]. The as-solidified morphology results from the competition between the nucleation of new equiaxed grains on partially melted powder particles and the pool-bottom epitaxial growth of large

*Corresponding author
mathieu.marquer@univ-lorraine.fr (M. Marquer); pascal.laheurte@univ-lorraine.fr (P. Laheurte); laurent.faure@univ-lorraine.fr (L. Faure); sylvain.philippon@univ-lorraine.fr (S. Philippon)
ORCID(s):

© 2020 published by Elsevier. This manuscript is made available under the CC BY NC user license
https://creativecommons.org/licenses/by-nc/4.0/

columnar grains [15]. The < 100 > fibre solidification growth direction was reported to tend to be aligned with the direction of the maximum thermal gradient that corresponds to the SLM built direction [16]. In as-built SLM specimens, columnar grains correspond to cubic β grains. Upon cooling, β phase transforms into α'-martensite in the case of a high cooling rate and to α in the case of a low cooling rate [16]. The martensitic final microstructure (high cooling rate) is the one typically observed, and is characterized by large, elongated prior β-phase grain boundaries that are filled with very fine acicular α' martensite [17]. This microstructure have been studied by means of EBSD [13, 18, 11], showing that the variants of α' grains are selected by the prior β-grains, which explains why the β-grains boundaries are inherited between the regions of α' variants formed.

Some studies discuss the influence of SLM manufacturing Ti6Al4V parts on their tribological behaviour in mild conditions. Most have been done in the context of biomedical applications and were thus performed in lubricated conditions, using artificial body fluid, for example. They showed little to no influence of the process on the friction coefficient, despite SLM Ti6Al4V having a markedly improved wear resistance when compared to cast Ti6Al4V [19, 20]. This improvement of wear resistance is explained by the higher hardness of Ti6Al4Vparts manufactured by SLM.

In dry conditions, Li *et al.*[21] showed that SLM, EBM, and conventional Ti6Al4V had similar friction coefficient and wear despite very different hardnesses. They explained this fact by the role of ductility, which decreases when hardness increases, in the formation of wear. Chandramohan *et al.* showed in a first study [22] that the wear volume depends on the orientation of the building direction of the part at low, but not at medium and high, load. In a second publication [23], they showed that heat treatment had more influence on the wear resistance of SLM-manufactured parts than their orientation.

The tribological behaviour of SLM-Ti6Al4V in severe conditions had yet to be investigated. Hence, the aim of this investigation is to compare the tribological behaviour of 3D-printed (SLM) parts to machined ones under severe loading conditions. For this purpose, we consider an application such as a bird ingestion by a jet engine wherein one part (e.g. the blade) is obtained by standard processes while the counterpart (e.g. the disk) is obtained by either SLM or standard processes.

The scope of this work was limited to the study of the evolution of the friction coefficient and wear. The variables were the counterpart material (machined or produced by SLM with different building orientations) and the contact pressure (110 or 300 MPa). The sliding speed was fixed at 40 m/s and the moving part was made of machined Ti6Al4V.

2. Materials and methods

2.1. Friction test

Several kinds of devices are available for tribological studies, depending on the test conditions considered. In this work, the main constraints were the sliding speed ($v = 40\,\mathrm{m/s}$) and the apparent pressure range ($110\,\mathrm{MPa} < p < 300\,\mathrm{MPa}$). A moderate (less than 100 mm) but not too short (more than 1 mm) sliding distance was also necessary, as well as a quasi-absence of running-in period. In order to satisfy these constraints, a slider-on-pad setup was used.

The slider-on-pad tribometer was first designed by Philippon [24] and was later successively enhanced. In this work, the fourth version of this device, adapted to a ballistic bench, is employed. This configuration is detailed in references [4, 6]. For the present experiments, the setup and procedure described in [6] were used.

For each experiment, a set of three specimens was used: one slider and two pads. After placing the slider of length L_S in-between the pads of length L_P (see Fig. 1), the normal force is applied on the stack by a dynamometer ring. Its stiffness $k_{DR} = 24\,\mathrm{kN/mm}$ results from its elastic behaviour. The slider is then impacted by a heavy ($m_P = 550\,\mathrm{g}$) steel projectile, causing it to accelerate in less than 50 µs [25] to a speed called "initial sliding speed" v_i.

This projectile is launched by a reservoir-type gas-gun. The launching parameters resulting in the chosen initial sliding speed value ($v_i = 40\,\mathrm{m/s}$) were determined in calibration tests performed prior to this work (see appendix A for the calibration process and accuracy calculations). Thanks to this calibration and to the good repeatability of the initial sliding speed ($\leq \pm 1\,\mathrm{m/s}$ at $40\,\mathrm{m/s}$), it was not necessary to measure the initial sliding speed of the tests presented in this paper.

During the experiment, the normal force F_N and both tangential forces F_{T1} and F_{T2} (cf. Fig. 1) resulting from the friction on each pad are recorded. An average friction force F_T is calculated from F_{T1} and F_{T2}. The interaction can be divided into 3 main stages which are highlighted in Figs. 1 and 2. At the beginning (phase 1), the projectile impacts the slider which starts moving. The inertia effects cause a peak of tangential force. After this transient period ($t \geq t_1 = 400\,\mu\mathrm{s}$), the system is in a relatively steady state (phase 2). Once the end of the slider has reached the pads ($t \geq t_2$, where $L_\mathrm{S} - L_\mathrm{P} = \int_0^{t_2} v(t) \cdot dt$), the contact area decreases, causing the apparent contact pressure to increase.

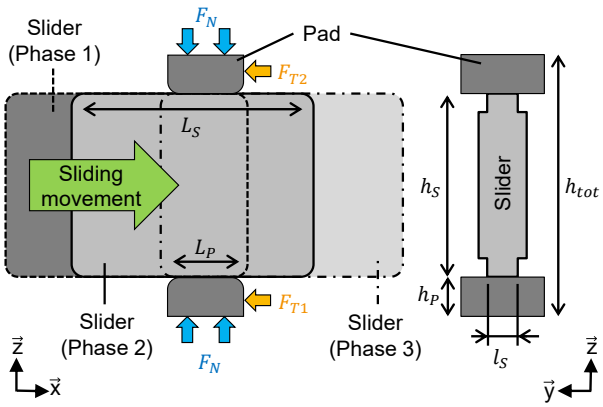

Figure 1: Samples configuration

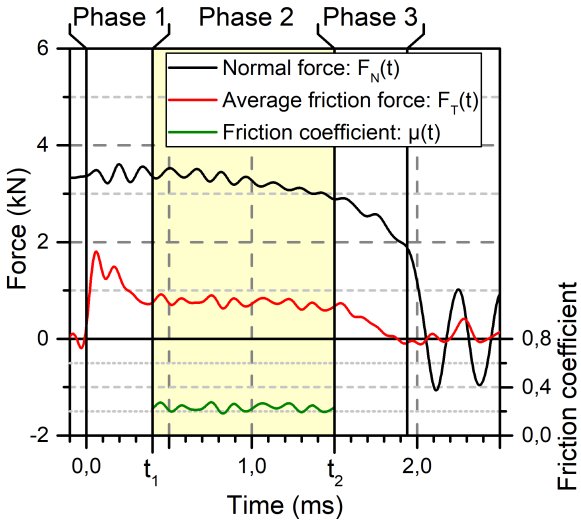

Figure 2: Typical recording (test with machined Ti6Al4V pads at $v_i = 40\,\mathrm{m/s}$ and $p = 110\,\mathrm{MPa}$)

Due to this increased compressive stress, the stack thickness h_{tot} decreases. This is the beginning of the third phase, which ends when the slider is no longer in contact with the pads ($t = L_S/v$).

Given the nature of phases 1 and 3, only the second phase is considered for calculating the friction coefficient. From the normal and average friction forces, a coefficient of friction $\mu(t) = F_T(t)/F_N(t)$ is calculated (Coulomb's law). The average value $\overline{\mu}$ (Eq. 1) is used as the test friction coefficient.

$$\overline{\mu} = \frac{1}{t_1 - t_2} \cdot \int_{t_1}^{t_2} \mu(t) \cdot dt \tag{1}$$

As the normal force is applied through a dynamometer ring, this force depends on the total thickness h_{tot} of the samples ($h_{tot} = 2\,h_P + h_S$). The part of the slider involved in the sample stack is constantly renewed during sliding, therefore its thickness h_S is constant during the interaction process. However, the thickness h_P of the pads decreases during the test (e.g. due to wear). A slow decrease of the normal force F_N is hence typically observed during the interaction (Fig. 2).

After the friction tests, the slider, projectile, and pads were retrieved in a receiver tank filled with shock-absorbing material in order to dissipate the kinetic energy of the parts. The wear volume of the pads was then calculated from their

Table 1
Friction and SLM axes correspondence for each pad type

Name of the friction test axis		SLM pad type A	B	C
Sliding	$\vec{x}$	$-\vec{N}$	$\vec{T}_2$	$-\vec{T}_2$
Transversal	$\vec{y}$	$\vec{T}_2$	$\vec{N}$	$\vec{T}_1$
Loading	$\vec{z}$	$\vec{T}_1$	$\vec{T}_1$	$\vec{N}$

topography (measured by focus-variation microscopy). This process is described in details in a previous publication [6] to which the reader may refer for details pertaining to this step. This publication also details why measuring the wear of the slider was not possible. For a friction test, the wear volume w is the mean value of the apparent wear of the two pads.

All friction tests were performed twice for each configuration.

2.2. Materials

2.2.1. Fabrication of the samples

As mentioned in section 2.1, each test uses one slider and two pads. This study uses only one kind of slider and four kinds of pads. The slider (S) and one kind of pad (M) were machined from manufacturer-bought Ti6Al4V. The last machining step was the grinding of the contact surface. The three other kinds of pads were made by selective laser melting (SLM), with the orientations defined in Fig. 3a. For each kind of SLM pad, the building axes matched different friction test axes, presented Fig. 3b and Tab. 1.

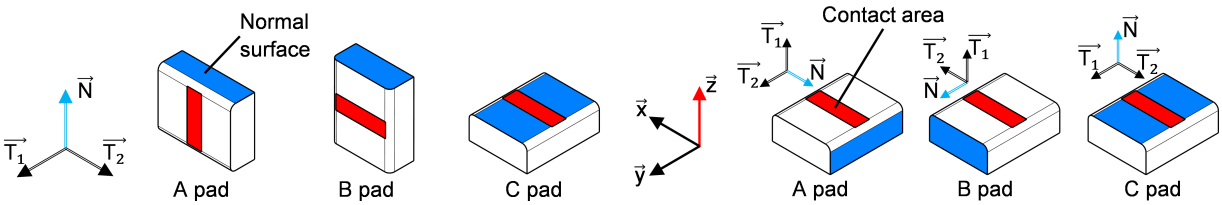

(a) SLM (building) configuration (b) Friction test configuration

Figure 3: Orientation of the SLM pads during a) manufacturing and b) friction test

The samples were manufactured using an SLM 280 HL (SLM Solutions) machine, with the scanning strategy presented Fig. 4. The back-and-forth (or "meander") scanning pattern of each successive layer was turned by $\Delta\theta = 67°$ from the previous one, leading to a 180 layers distance between two patterns with the same direction. This is sometimes called a "Meander 67°" strategy [26, 27, 27, 28]. The samples were produced under argon atmosphere from a Ti6Al4V powder of spherical particles, with a particle size centered on 45 µm ranging from 15 to 63 µm. The detailed SLM parameters are listed in Tab. 2 and were chosen as recommended by the machine manufacturer.

(a) Layering (b) Angular pattern orientation

Figure 4: Building strategy of the SLM samples: the scanning pattern of each layer a) is turned 67° from the previous one in order to minimize overlapping b)

Table 2
Process parameters used for the manufacturing of the SLM parts

Process parameters	Value	Unit
Powder material	Ti6Al4V	
Powder size	−53 +20	µm
Atmosphere	Argon	
Laser power	200	W
Spot size	60	µm
Scan speed	1 175	mm/s
Pattern type	Meander	
Hatch distance	80	µm
Pattern rotation	67	°
Layer thickness	35	µm

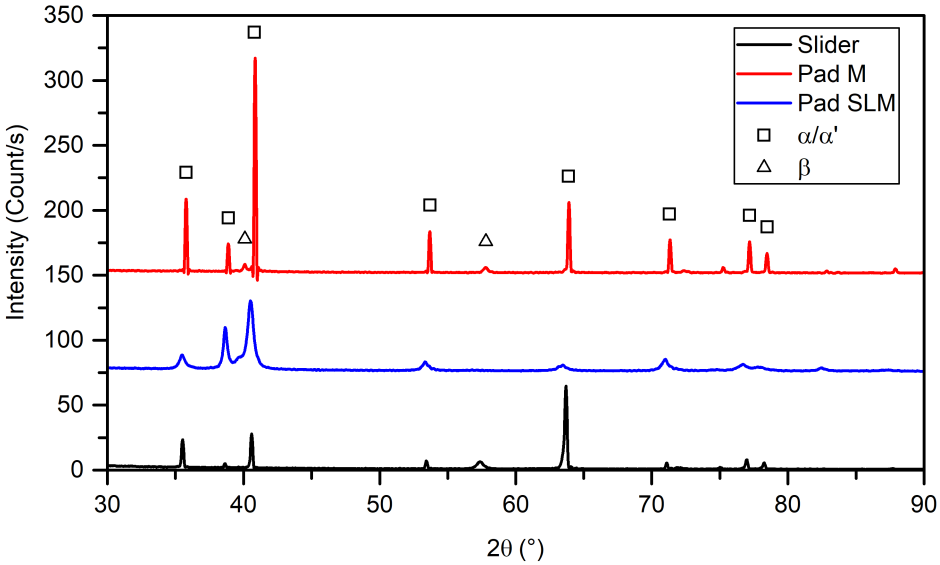

Figure 5: XRD (X-ray diffraction) patterns for Ti6Al4V alloy obtained in the SLM (blue) and annealed samples (black and red)

The aim of this work was to compare samples manufactured through subtractive (i.e. machining) and additive (i.e. SLM) manufacturing techniques in their "as received" state. Hence, the friction face of the SLM pads was only cleaned by means of ethanol. For SLM pads, parallelism between the dynamometer ring and the friction face of the pad was ensured by face-milling the face of the pad opposite to the friction face.

2.2.2. Samples properties

The properties of parts made by SLM can vary depending on the orientation of the part relative to the SLM table. Furthermore, Ti6Al4V tends to have an anisotropic microstructure and can therefore exhibit anisotropic mechanical properties.

To test whether the orientation of the pad during the SLM process had any influence on its properties as a whole, its microstructure needs to be evaluated. For that purpose XRD measurements were carried out with a Siemens D5000 diffractometer fitted with a copper anode (wavelength 0.154 nm) (Fig. 5). For the slider and annealed pad (M), a very small amount of beta phase was detected, while for the SLM pad, the peaks were assigned to hcp titanium (α' martensite). The martensitic microstructure of the SLM pad showed little to no texture at a macroscopic scale.

The hardness was measured for the SLM and M pads, as well as for the S slider. A Buehler Micromet 5114 Digital Macro Vickers hardness tester (1 kgf-50 kgf) was used for these measurements. They were performed under a 10 kgf

load in the xz cross-section of each part. The measurements of the SLM pads are designated by the loading axis of the measurement. For example, for the measurements taken on the T_1T_2-plane, the load was applied along the N axis and the result is called HV_N. For each cross-section, at least 5 measurements were taken.The samples exhibit reasonable homogeneity in the distribution of their hardness results, presented Fig. 6.

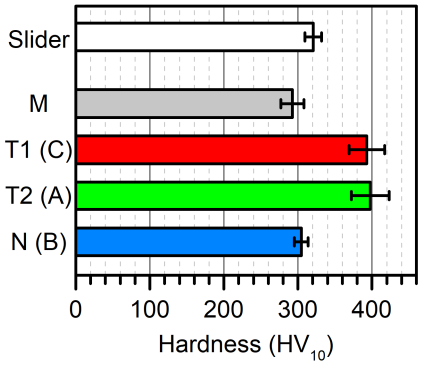

Figure 6: Vickers hardness (HV_{10}) results. For SLM pads, both the measurement direction (i.e. N, T_1, and T_2) and the pad designation (i.e. A, B, and C) are given

The HV values for T_1 and T_2 (average: $\approx$ 395 HV) are higher than that of N (average: $\approx$ 304 HV), indicating anisotropy in SLM Ti6Al4V between the two build orientations. Several studies have identified possible causes for anisotropy in additively manufactured materials, including the level of defects, residual stress, local heat transfer conditions, scan strategy, grain orientation, and to a lesser extent, crystallographic texture [29]. The hardness of the SLM materials is lower in the direction perpendicular to layers (axis N, here) [30, 31]. Since the HV values for T_1 and T_2 are close, it is apparent that the SLM-Ti6Al4V used is transversely isotropic of axis N. This is coherent with the typical as-built microstructure of SLM Ti6Al4V described in section 1. Indeed, while the microstructure shows little to no texture at a macroscopic scale, it is structured in regions of α' variants. Their boundaries are inherited from the parent columnar β-grains, which may give the material the transversely isotropic behaviour of a columnar microstructure.

In the literature it is often noted that the hardness of the structures obtained after additive manufacturing is greater than obtained by casting. This is partially the case here, since HV_{T1} and HV_{T2} are higher than HV_M, but HV_N and HV_M are close.

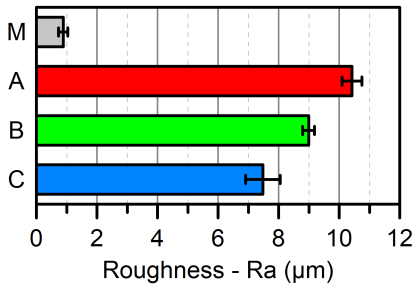

Figure 7: Arithmetic pad roughness (Ra)

As explained in the previous section (2.2.1), the pads were used in their "as received" state, whether obtained through subtractive (i.e. machining) or additive (i.e. SLM) manufacturing techniques. For that reason, they have a different micromorphology from one another which can be observed in appendix B. The tribological behaviour of the contact is however not expected to be influenced by roughness, as mentioned in section 1. Roughness measurements were performed according to EN ISO 4288, using an Alicona Infinite Focus focus variation microscope. The results (Fig. 7) show a marked difference between the two techniques with subtractive samples having an arithmetic roughness $Ra = 0.89 \pm 0.15$ µm, which is nearly ten times smaller than that of additive ones (7.48 µm $\leq Ra \leq$ 10.42 µm). Among

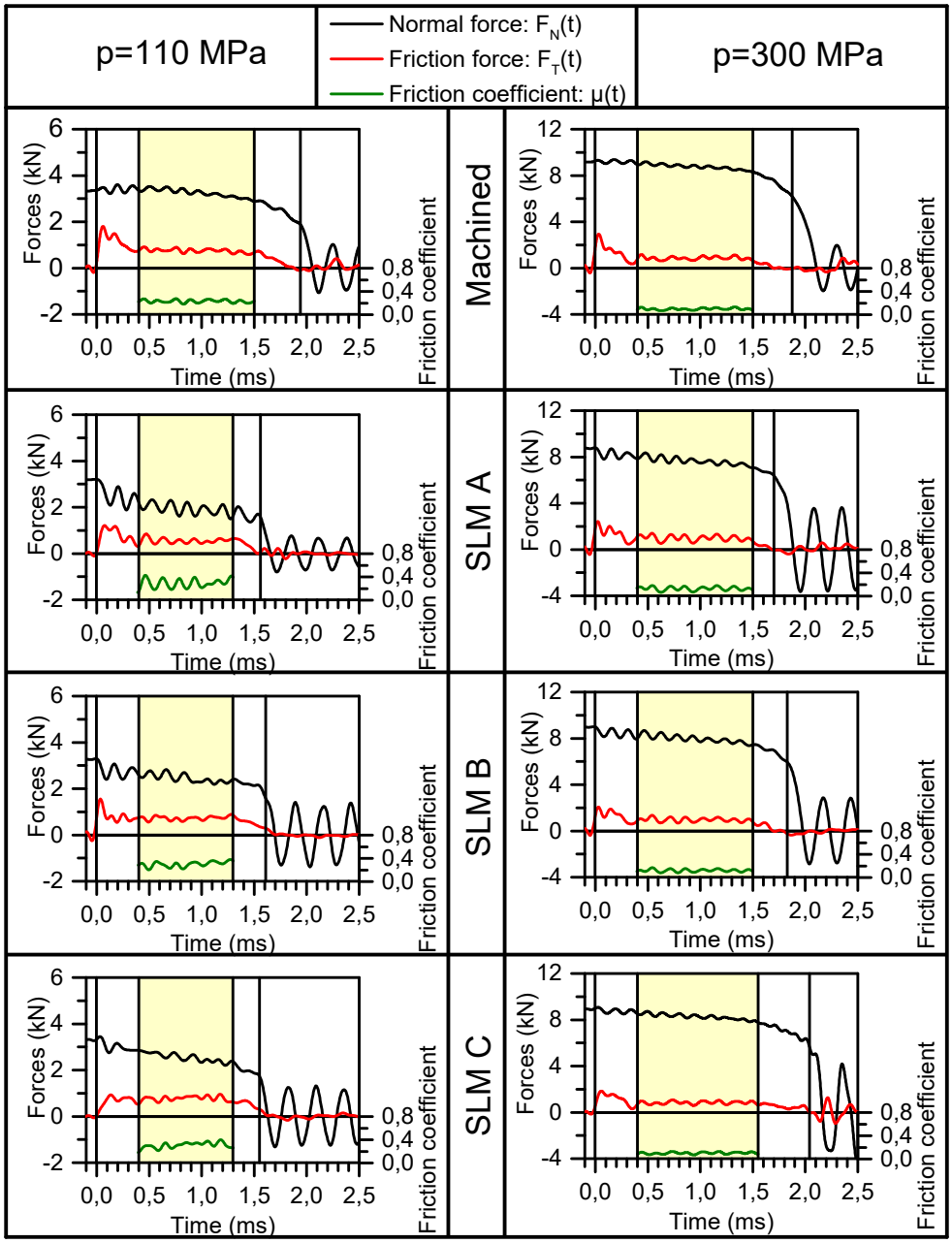

Figure 8: Typical recording for each test configuration: (pad type and initial apparent pressure)

the SLM samples, roughness was observed to vary depending on the type of sample. The roughness produced on the horizontal face (samples C) was the smallest with $Ra = 7.48 \pm 0.57\,\mu m$. The lateral faces presented a roughness of $Ra = 8.99 \pm 0.20\,\mu m$ along the building direction (samples A) and $Ra = 10.42 \pm 0.33\,\mu m$ along the transversal direction (samples B).

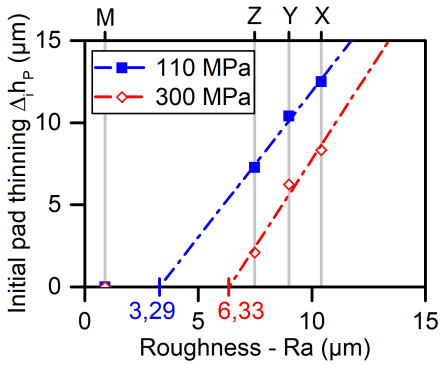

Figure 9: Initial pad thinning $\Delta_i h_P$ compared to the initial arithmetic roughness Ra

3. Results and Discussions

3.1. Recordings

The typical signals ($F_N(t)$ and $F_T(t)$) obtained for each of the test configurations, as well as the corresponding friction coefficient $\mu(t)$ for phase 2, are presented Fig. 8. The resulting values of the average friction coefficient $\overline{\mu}$ are represented Fig. 11a. The reference configurations (machined samples) present signals similar to those obtained in previous studies [4, 32].

For all configurations, a slow decrease of the normal force F_N is observed. As described in section 2.1, this is mainly caused by the progressive wear of the pads. For the configurations with SLM pads, however, an initial drop $\Delta_i F_N$ in the normal force value is also observed, most notable in tests at $p_i = 110$ MPa. In these tests, the initial drop is of a few hundreds of newtons, with approximate values of 600 N, 500 N and 350 N (18 %, 15 % and 11 % of the initial normal force) for A, B, and C respectively. Considering that the force is applied by a dynamometer ring of stiffness k_{DR}, this can be converted into a per-pad thickness variation $\Delta_i h_P$ of 25 µm, 21 µm and 15 µm (Eq. 2).

$$\Delta_i h_P = \frac{\Delta_i F_N}{2 \cdot k_{DR}} \tag{2}$$

This initial thinning could reasonably be attributed to a flattening of the relatively high initial roughness of the SLM pads. In that case, a positive correlation is expected to exist between the initial roughness and initial thinning. To put this hypothesis to the test, Fig. 9 compares $\Delta_i h_P$ to the arithmetic roughness of the sample. $\Delta_i h_P$ indeed seems to be strongly dependent on Ra, with $\Delta_i h_P = 1.70\,Ra - 5.83$ ($R^2 > 0.99$) at $p_i = 110$ MPa. Similarly, at $p_i = 300$ MPa, the initial drops in normal force are 400 N, 300 N and 100 N (5 %, 3 % and 1 % of the initial normal force) for A, B and C respectively. This is equivalent to a thinning $\Delta_i h_P$ of 8.3 µm, 6.3 µm and 2.1 µm which gives $\Delta_i h_P = 2.12\,Ra - 13.4$ ($R^2 > 0.96$).

From these equations, the minimum arithmetic roughness needed to observe an initial drop in normal force F_N is $Ra_T = 3.3$ µm at $p_i = 110$ MPa and $Ra_T = 6.3$ µm at $p_i = 300$ MPa. This threshold Ra_T represents the limit of the ability of the surface asperities to withstand the stresses applied to them when friction is initiated.

A mechanism that would explain the previous observations is presented Fig. 10. Above the threshold roughness, the asperities are too slender and collapse under a deviated compressive load (a compressive load applied to the deformed asperity), in a phenomenon known in civil engineering as "P-Delta collapse" [33]. Below Ra_T, the asperities are stout enough to tolerate the load deviation resulting from the shear strain. When the samples are in contact under an apparent pressure p, the actual roughness decreases as p increases, which explains the increase of Ra_T with p_i.

This mechanism is dependent on both the shape of the asperities and their mechanical properties. It is important to highlight that in this work Ra was the only roughness parameter measured. While it can reasonably be expected that an increase in Ra would mean an increase in slenderness of asperities, this is not what this parameter is designed to measure. SLM processing parameters could also influence the properties of the asperities. Modifying them could therefore alter the observed behaviour.

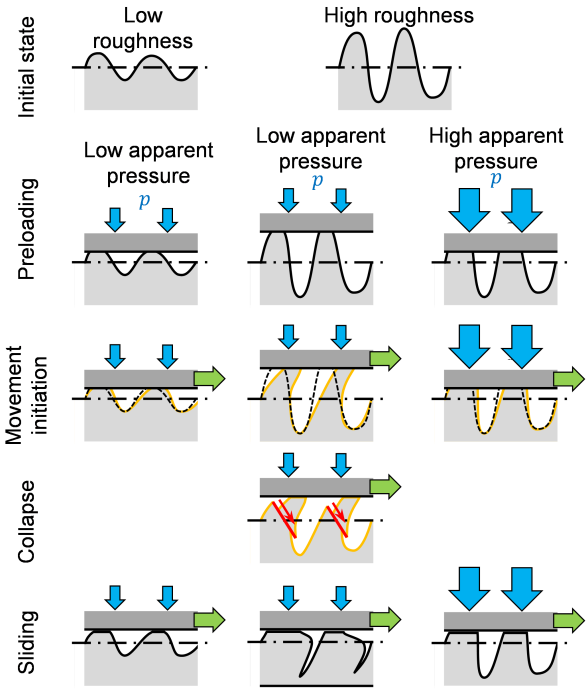

Figure 10: Influence of roughness and apparent pressure on asperity collapse

Summary: In this section, we observed that an initial drop in normal force was present in the tests with SLM pads and linked it to an initial drop in pad thickness that we called "initial thinning". As this thinning seemed correlated to both roughness and initial apparent pressure, a mechanism based on "P-Delta collapse" was proposed to explain it. Complementary studies will however be needed to confirm the validity of the proposed mechanism.

3.2. Friction coefficients and apparent wear

The average friction coefficients for M match results from previous studies. At $v_i = 40\,\mathrm{m/s}$ and $p_i = 110\,\mathrm{MPa}$, Chassaing *et al.* [4] measured the friction coefficient to be 0.19 ± 0.03. This matches the present 0.228 ± 0.004 result for this configuration. At 300 MPa, the present results (0.096 ± 0.004) are slightly higher than theirs (0.08) but they are still reasonably similar.

At $p_i = 110\,\mathrm{MPa}$, the average friction coefficient $\overline{\mu}$ (Fig. 11a) only presents a marginal difference between the average values for each orientation. It is maximal between A (0.308 ± 0.016) and B (0.334 ± 0.035). At $p_i = 300\,\mathrm{MPa}$, the variation of $\overline{\mu}$ between the different SLM orientations is even smaller, being maximal between B (0.126 ± 0.005) and C (0.117 ± 0.015). Whether at 110 or 300 MPa, there is also a significant overlap between the friction coefficients measured for all SLM orientations (error bars of Fig. 11a). It can therefore be concluded that for the average friction coefficient $\overline{\mu}$ is generally insensitive to the orientation of the pad relative to the SLM machine.

There is a significant difference between the friction coefficients corresponding to tests with machined pads and the ones corresponding to tests with SLM pads. With $0.095^{+0.050}_{-0.035}$ (0.228 ± 0.004 for M and $0.323^{+0.046}_{-0.031}$ for SLM), this difference is higher at $p_i = 110\,\mathrm{MPa}$ than at $p_i = 300\,\mathrm{MPa}$ where its value is $0.025^{+0.015}_{-0.023}$ (0.096 ± 0.004 for M and $0.121^{+0.011}_{-0.019}$ for SLM).

At $p_i = 110\,\mathrm{MPa}$, the type of SLM pad has little influence on the wear volume w (Fig. 11b). The maximal difference is recorded between A ($0.78 \pm 0.04\,\mathrm{mm}^3$) and C ($0.85 \pm 0.05\,\mathrm{mm}^3$). Machined pads, however, present a significantly larger wear volume than SLM ones: $w = 1.00 \pm 0.12\,\mathrm{mm}^3$ At $p_i = 300\,\mathrm{MPa}$, the variation of w between the different SLM orientations increases, but so does the dispersion, with still largely overlapping uncertainties: the maximal difference is $0.18 \pm 0.24\,\mathrm{mm}^3$ between A ($1.55 \pm 0.20\,\mathrm{mm}^3$) and C ($1.37 \pm 0.04\,\mathrm{mm}^3$). It can therefore neither be said that wear is insensitive to SLM orientation nor that it is not. It is however possible to affirm that pads from C and M exhibit the same wear.

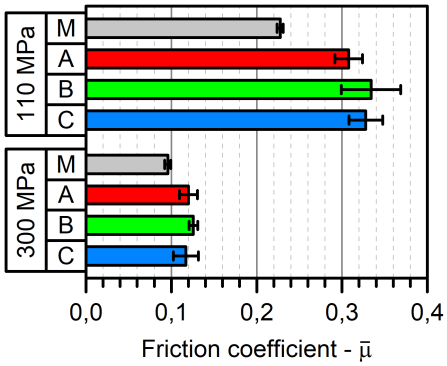

(a) Average friction coefficient $\overline{\mu}$

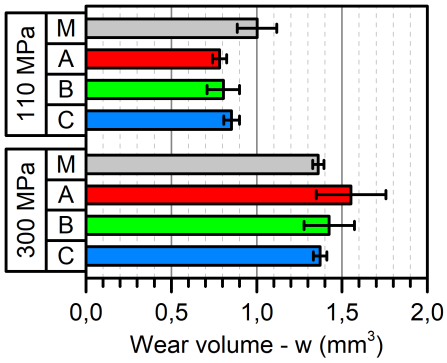

(b) Average wear volume w

Figure 11: Summary of the main results for each initial apparent contact pressure and pad material

Summary: In the specific configurations tested in this study, tests with SLM pads had an average friction coefficient $\overline{\mu}$ higher than that of tests with machined pads. A 40 % increase in average friction coefficient was observed at $p_i = 110$ MPa, lowered to about 30 % at $p_i = 300$ MPa. At $p_i = 110$ MPa, the use of SLM pads of any orientation lowered wear volume by about 20 %. No difference was observed between M and C at $p_i = 300$ MPa, but no conclusion could be reasonably reached about A and B.

3.3. Influence of the apparent contact pressure during phase 2

As can be deduced from its name, the initial apparent pressure p_i is not the actual apparent contact pressure during the useful phase of the test (phase 2, see section 2.1). There is no significant discrepancy for M tests (less than 5 %). However, SLM tests were much more affected. Due to the initial thinning and wear, the actual test pressure was lower by a notable margin (up to 40 %) for the SLM tests at $p_i = 110$ MPa. As highlighted in section 1, friction coefficient and wear can be quite sensitive to apparent contact pressure. Using p_2, the average of the apparent contact pressure during phase 2, Fig. 12 represents the results for each individual test (grouped by pad material and initial contact pressure in Fig. 11). For the purpose of comparison, results from [5] for a Ti6Al4V-Ti6Al4V couple at $v_i = 40$ m/s are also presented. This reference configuration is henceforth designated as M.ref.

The results from the present study, when combined, seem to follow a trend similar to that of M.ref. They are however higher by approximately 50 %. As emphasized in section 2.1, the initial sliding speed was highly repeatable and could not have deviated by more than 1 m/s from the target speed. Furthermore, a difference in pad microstructure between M and M.ref could not have been starker than between SLM and M pads (section 2.2.2). Given how this result seems to form a single curve from such dissimilar pad microstructures, the difference in pad microstructure between M and M.ref could not have caused the observed difference.

A difference in slider microstructure could however influence the friction coefficient results. Chassaing *et al.* [4] showed that the contact mechanisms were mainly driven by the pad. Marquer *et al.* [6] confirmed that observation but

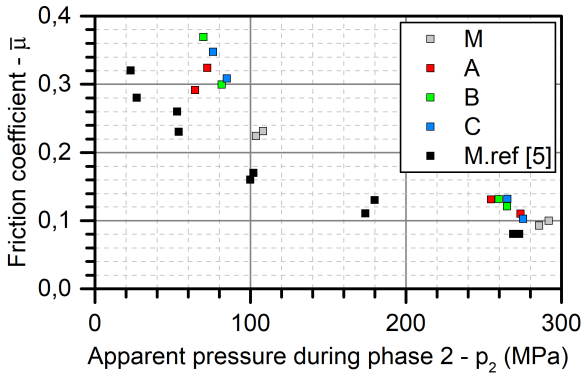

Figure 12: Friction coefficient as a function of the average apparent pressure during phase 2 (p_2)

also showed that the thermomechanical behaviour of the slider was crucial as well, and could, in certain conditions, be the main driver of the friction coefficient. It was especially demonstrated that the thermal properties of the parts were of great influence on the activated tribological mechanisms.

Despite the variation discussed above, the main takeaway is that whether SLM or machined pads are used, the friction coefficient seems to follow the same trend, similar to the one observed in the reference work with machined pads only. Due to the limited number of configurations, it is necessary to highlight the need for complementary tests to have results at the same average apparent pressure p_2.

Summary: Initial thinning with SLM pads led to a reduced apparent contact pressure during the tests (p_2). The evolution, relative to p_2, of the aggregated friction coefficients of all tests (SLM and machined pads) was similar to that found in the literature. However, the friction coefficients were higher, which could be caused by the counterpart. Complementary tests may be needed to complete that observation.

3.4. Energetic approach to pad wear

Wear is often considered to not simply be a speed or pressure-activated phenomenon, but an energy-driven one. Various studies have shown a linear link (Eq. 3) between wear w and dissipated energy E_D [34, 35, 36, 37]. Jahangiri *et al.* [37] designate the ω coefficient as the "specific wear volume" (unit: mm^3/J) and define the dissipated energy as the cumulative friction work dissipated at a given wear distance (Eq. 4).

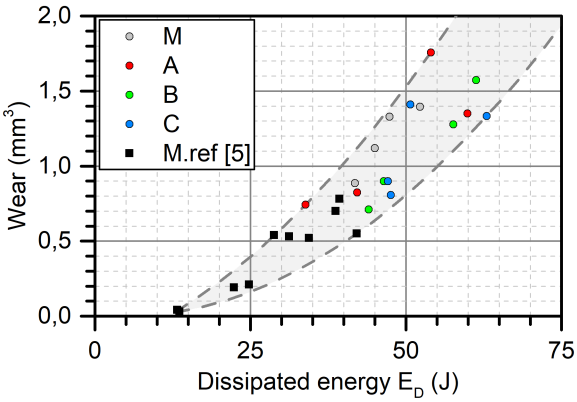

Figure 13: Wear volume w as a function of dissipated energy E_D

$$w = \omega \cdot E_D \tag{3}$$

$$E_D = \int_{start}^{end} F_T dx \tag{4}$$

Assuming that the friction force F_T remains constant during the test, $E_D = F_T \cdot L_S$, where $F_T = \overline{\mu} \cdot p_2 \cdot S$, giving Eq. 5 for an approximation of E_D.

$$E_D = \overline{\mu} \cdot p_2 \cdot S \cdot F_T \cdot L_S \tag{5}$$

Fig. 13 represents the wear as a function of the dissipated energy. The M.ref reference data ($\overline{\mu}$ and w at $v_i = 40\,\mathrm{m/s}$) were extracted from [5] and processed using Eq. 5 to obtain E_D.

While SLM results are a bit more scattered than M.ref and M, a single trend seem to be followed by all combined results. This indicates that energy dissipated by friction causes the same amount of wear whether the pad has been machined or produced by SLM. Results are however a bit too scattered to be able to reliably extract the specific wear volume ω. Furthermore, contrary to the hypothesis, w does not seem to follow a linear progression.

Summary: As wear is considered to be energy-driven, wear volume for all configurations tested in the present study, as well as for tests from the literature done in similar conditions was plotted relative to friction-dissipated energy. No matter the type of pad, wear for all tests followed a single trend.

4. Conclusion

The aim of this research was to compare the behaviour of 3D-printed (SLM) and machined parts under severe tribological loading conditions. The evolution of the friction coefficient and that of wear as a function of both the counterpart material (machined or produced by SLM with different orientations) and the contact pressure (110 or 300 MPa) were studied. The initial sliding speed was 40 m/s and the moving part was machined Ti6Al4V.

The following elements were highlighted:

- The average friction coefficient $\overline{\mu}$ was mostly independent from SLM orientation.
- Tests with SLM pads had an average friction coefficient $\overline{\mu}$ higher by 30 % (at $p_i = 300$ MPa) to 40 % (at $p_i = 110$ MPa) than with machined pads.
- At $p_i = 110$ MPa, SLM pads had a 20 % lower wear volume than machined ones. This was observed whatever the SLM orientation.
- At $p_i = 300$ MPa, no difference was observed between M and C but no conclusion could reasonably be reached about A and B.
- Initial thinning for SLM is strongly correlated to initial pad roughness and initial apparent pressure. We propose that the initial thinning is caused by asperity collapse under deviated load due to asperity slenderness.
- Initial thinning with SLM pads led to a reduced apparent contact pressure during the tests (p_2). The evolution, relative to p_2, of the aggregated friction coefficients of all tests (SLM and machined pads) was similar to that found in the literature [5]. The friction coefficients were, however, higher by about 50 %, which we propose is due to the counterpart.
- No matter the type of pad, wear for all tests of the present paper, as well as for tests done in a similar setting with conventionally produced pads, followed a single trend relative to friction-dissipated energy.

Given these conclusions, and other information present in this work, further investigations of the behaviour of SLM Ti6Al4V under severe tribological loading conditions should focus on three main elements:

- Complementing the present dataset with tests at $p_2 = 110$ MPa for SLM pads. Using the relationship between initial pad roughness and initial thinning could be a useful tool.

- Studying the evolution of the pads and slider microstructures. The mechanically and heat-affected zones of the slider and the pad have proven to be reliable tools for understanding tribological phenomena at the contact interface [6, 4].
- Studying the influence of post-SLM treatments (machining and/or stress relieving heat treatments) on the behaviour of the parts.

Additionally, the initial thinning mechanism proposed should be validated by a specifically designed study, which should account for the remarks made in section 3.1.

5. Acknowledgments

We are grateful to Mr Franck DUCOS, from the IUT of Moselle-Est (Forbach, France), for performing the hardness measurements used in this study.

This research did not receive any specific grant from funding agencies in the public, commercial, or not-for-profit sectors.

6. Appendices

A. Accuracy of the initial sliding velocity for a reservoir-type gas-gun

A.1. Projectile velocity

The projectile is launched horizontally by a reservoir-type gas-gun. In this type of device, the energy of a gas (here, air) initially stored at a pressure p_R in a reservoir of volume V_R, is used to accelerate the projectile along a barrel of volume V_B. The muzzle velocity v_P^m of the projectile is expressed by Eq. 6 and depends on the geometrical parameters of the launcher (V_R,V_B), on the gas properties (through its Laplace's coefficient γ), on the mass m_P of the projectile, on the pressure p_R in the reservoir, and on an energy transfer efficiency parameter η. This efficiency parameter η depends on various factors such as projectile-tube leaks and friction losses in the tube and valve [38].

$$v_P^m = \eta \sqrt{\frac{p_R}{m_P}} \sqrt{\frac{2\,V_R}{\gamma - 1}\left[1 - \left(\frac{V_R}{V_R - V_B}\right)^{\gamma-1}\right]} \tag{6}$$

The gas-gun parameter ζ is defined by Eq. 7, leading to the formulation Eq. 8 of the muzzle velocity equation.

$$\zeta = \eta \sqrt{\frac{2\,V_R}{\gamma - 1}\left[1 - \left(\frac{V_R}{V_R - V_B}\right)^{\gamma-1}\right]} \tag{7}$$

$$v_P^m = \zeta \sqrt{\frac{p_R}{m_P}} \tag{8}$$

The ζ parameter is calibrated prior to each test campaign in order to ensure maximum accuracy in the target speed range. This is done in three steps:

1. A projectile is launched with a pressure set from a rough estimation with values from previous launches, and measuring both m_P, p_R and v_P^m.
2. The ζ parameter is calculated from Eq. 8.
3. A projectile is launched with a pressure set from the calculated ζ value, measuring both m_P, p_R and v_P^m. This step ensures the validity of the ζ value.

The reservoir filling system allows the pressure to be set with an accuracy better than $\pm 5\,\%$. The muzzle speed is therefore set with a $\pm 2.5\,\%$ accuracy.

A.2. Initial sliding speed

The initial sliding speed of the slider is mostly independent from the friction coefficient between the slider and the pads. The energy balance of the projectile impacting the slider is given by Eq. 9. The initial sliding speed therefore depends on the muzzle and residual (after impact) speeds v_P^m and v_P^r of the projectile, the masses of the projectile and of the slider (m_P and m_S respectively), and the impact energy loss ΔE_{imp}.

$$\frac{1}{2} m_S \cdot v_i^2 = \frac{1}{2} m_P \left({v_P^m}^2 - {v_P^r}^2 \right) - \Delta E_{imp} \tag{9}$$

As can be demonstrated from [39, 40], the sensitivity of v_i to v_P^m decreases as v_P^m increases (mostly due to the ΔE_{imp} term). This leads to a very good repeatability of the initial sliding speed, even better than the $\pm 2.5\,\%$ projectile muzzle speed accuracy.

The projectile velocity (v_P^m) resulting in the chosen initial sliding speed value ($v_i = 40\,\mathrm{m/s}$) was determined in calibration tests performed prior to this work. During these tests, an ultra-high-speed camera (Shimadzu HPV2) was used to measure v_i. This calibration and the accuracy of the muzzle speed of the projectile lead to the good repeatability of the initial sliding speed ($\leq \pm 1\,\mathrm{m/s}$ at $40\,\mathrm{m/s}$).

B. Micromorphology of the pads

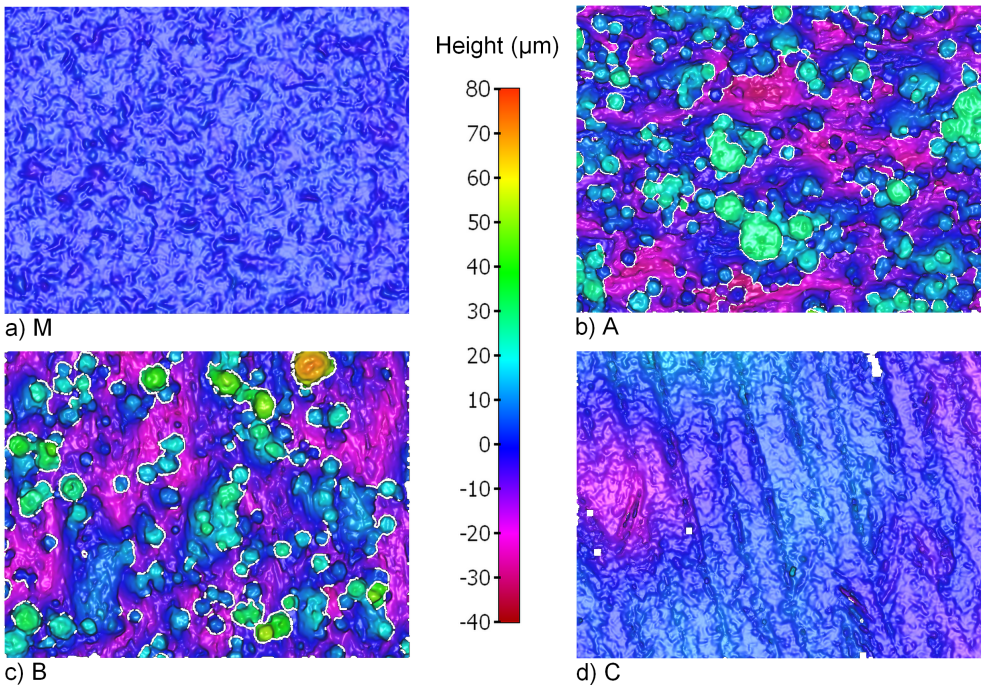

Figure 14: Altitude maps of all pads (field: $700\,\mu\mathrm{m} \times 540\,\mu\mathrm{m}$)

The micromorphologies of the friction surface of the pads before test are represented in figure 14. The maps were all obtained by focus-variation microscopy and represent an area of dimensions $700\,\mu\mathrm{m} \times 540\,\mu\mathrm{m}$. The altitude colour scale is the same for all images.

CRediT authorship contribution statement

Mathieu Marquer: Methodology, Formal analysis, Investigation, Writing - original draft, Writing - review & editing, Visualization. **Pascal Laheurte:** Conceptualization, Methodology, Investigation, Resources, Writing - original draft, Writing - review & editing. **Laurent Faure:** Conceptualization, Resources, Writing - review & editing. **Sylvain Philippon:** Conceptualization, Methodology, Resources, Writing - review & editing.

References

[1] Boyer, R.R.. An overview on the use of titanium in the aerospace industry. Mater Sci Eng A 1996;213(1-2):103–114. URL: http://linkinghub.elsevier.com/retrieve/pii/0921509396102331. doi:10.1016/0921-5093(96)10233-1.

[2] Whittaker, M.. Titanium in the Gas Turbine Engine. In: Benini, E., editor. Adv. Gas Turbine Technol.; vol. 4; chap. 14. InTech. ISBN 978-953-307-611-9; 2011, p. 315–336. URL: http://www.intechopen.com/books/advances-in-gas-turbine-technology/titanium-in-the-gas-turbine-engine.

[3] Budinski, K.G.. Tribological properties of titanium alloys. Wear 1991;151(2):203–217. URL: //www.sciencedirect.com/science/article/pii/004316489190249T. doi:http://dx.doi.org/10.1016/0043-1648(91)90249-T.

[4] Chassaing, G., Faure, L., Philippon, S., Coulibaly, M., Tidu, A., Chevrier, P., et al. Adhesive wear of a Ti6Al4V tribopair for a fast friction contact. Wear 2014;320(1-2):25–33. URL: http://www.sciencedirect.com/science/article/pii/S0043164814002592https://linkinghub.elsevier.com/retrieve/pii/S0043164814002592. doi:10.1016/j.wear.2014.08.001.

[5] Chassaing, G.. Frottement sec à grande vitesse du couple Ti6Al4V-Ti6Al4V : étude expérimentale et modélisation du comportement thermomécanique. Ph.D. thesis; Université de Lorraine; 2015. URL: https://tel.archives-ouvertes.fr/tel-01281680v1.

[6] Marquer, M., Philippon, S., Faure, L., Chassaing, G., Tardelli, J., Demmou, K.. Influence of two APS coatings on the high-speed tribological behavior of a contact between titanium alloys. Tribol Int 2019;136. URL: https://www-sciencedirect-com/science/article/pii/S0301679X19301501. doi:10.1016/j.triboint.2019.03.030.

[7] Marquer, M.. Etude comparative du comportement tribologique de revêtements frottant à grande vitesse sur un alliage de titane: CoCrAlYSiBN, CuNiIn, et MAO. Ph.D. thesis; Université de Lorraine; 2017. URL: http://www.theses.fr/s186506.

[8] Lim, S.C., Ashby, M.F., Brunton, J.H.. The effects of sliding conditions on the dry friction of metals. Acta Metall 1989;37(3):767–772. URL: http://www.sciencedirect.com/science/article/pii/0001616089900035. doi:http://dx.doi.org/10.1016/0001-6160(89)90003-5.

[9] Uhlmann, E., Kersting, R., Klein, T.B., Cruz, M.F., Borille, A.V.. Additive Manufacturing of Titanium Alloy for Aircraft Components. Procedia CIRP 2015;35:55–60. URL: http://www.sciencedirect.com/science/article/pii/S2212827115009154. doi:https://doi.org/10.1016/j.procir.2015.08.061.

[10] Huang, R., Riddle, M., Graziano, D., Warren, J., Das, S., Nimbalkar, S., et al. Energy and emissions saving potential of additive manufacturing: the case of lightweight aircraft components. J Clean Prod 2016;135:1559–1570. URL: http://www.sciencedirect.com/science/article/pii/S0959652615004849. doi:https://doi.org/10.1016/j.jclepro.2015.04.109.

[11] Liu, S., Shin, Y.C.. Additive manufacturing of Ti6Al4V alloy: A review. Mater Des 2019;164:107552. URL: http://www.sciencedirect.com/science/article/pii/S026412751830916X. doi:https://doi.org/10.1016/j.matdes.2018.107552.

[12] Zhao, X., Li, S., Zhang, M., Liu, Y., Sercombe, T.B., Wang, S., et al. Comparison of the microstructures and mechanical properties of Ti–6Al–4V fabricated by selective laser melting and electron beam melting. Mater Des 2016;95:21–31. URL: http://www.sciencedirect.com/science/article/pii/S0264127515309928. doi:https://doi.org/10.1016/j.matdes.2015.12.135.

[13] Simonelli, M., Tse, Y.Y., Tuck, C.. Effect of the build orientation on the mechanical properties and fracture modes of SLM Ti–6Al–4V. Mater Sci Eng A 2014;616:1–11. URL: http://www.sciencedirect.com/science/article/pii/S0921509314009538. doi:https://doi.org/10.1016/j.msea.2014.07.086.

[14] Sui, Q., Li, P., Wang, K., Yin, X., Liu, L., Zhang, Y., et al. Effect of Build Orientation on the Corrosion Behavior and Mechanical Properties of Selective Laser Melted Ti-6Al-4V. 2019. doi:10.3390/met9090976.

[15] Wang, T., Zhu, Y.Y., Zhang, S.Q., Tang, H.B., Wang, H.M.. Grain morphology evolution behavior of titanium alloy components during laser melting deposition additive manufacturing. J Alloys Compd 2015;632:505–513. URL: http://www.sciencedirect.com/science/article/pii/S0925838815003540. doi:https://doi.org/10.1016/j.jallcom.2015.01.256.

[16] de Formanoir, C., Michotte, S., Rigo, O., Germain, L., Godet, S.. Electron beam melted Ti–6Al–4V: Microstructure, texture and mechanical behavior of the as-built and heat-treated material. Mater Sci Eng A 2016;652:105–119. URL: http://www.sciencedirect.com/science/article/pii/S0921509315306420. doi:https://doi.org/10.1016/j.msea.2015.11.052.

[17] Thijs, L., Verhaeghe, F., Craeghs, T., Humbeeck, J.V., Kruth, J.P.. A study of the microstructural evolution during selective laser melting of Ti–6Al–4V. Acta Mater 2010;58(9):3303–3312. URL: http://www.sciencedirect.com/science/article/pii/S135964541000090X. doi:https://doi.org/10.1016/j.actamat.2010.02.004.

[18] Simonelli, M., Tse, Y.Y., Tuck, C.. On the Texture Formation of Selective Laser Melted Ti-6Al-4V. Metall Mater Trans A 2014;45(6):2863–2872. URL: https://doi.org/10.1007/s11661-014-2218-0. doi:10.1007/s11661-014-2218-0.

[19] Balla, V.K., Soderlind, J., Bose, S., Bandyopadhyay, A.. Microstructure, mechanical and wear properties of laser surface melted Ti6Al4V alloy. J Mech Behav Biomed Mater 2014;32:335–344. URL: http://www.sciencedirect.com/science/article/pii/S1751616113004128. doi:https://doi.org/10.1016/j.jmbbm.2013.12.001.

[20] Bartolomeu, F., Buciumeanu, M., Pinto, E., Alves, N., Silva, F., Carvalho, O., et al. Wear behavior of Ti6Al4V biomedical alloys processed by selective laser melting, hot pressing and conventional casting. Trans Nonferrous Met Soc China 2017;27(4):829–838. URL: http://www.sciencedirect.com/science/article/pii/S1003632617600608https://linkinghub.elsevier.com/retrieve/pii/S1003632617600608. doi:10.1016/S1003-6326(17)60060-8.

[21] Li, H., Ramezani, M., Chen, Z.W.. Dry sliding wear performance and behaviour of powder bed fusion processed Ti–6Al–4V alloy. Wear 2019;440-441:203103. URL: http://www.sciencedirect.com/science/article/pii/S0043164819310907. doi:https://doi.org/10.1016/j.wear.2019.203103.

[22] Chandramohan, P., Bhero, S., Obadele, B.A., Olubambi, P.A.. Effect of build direction on the microhardness and dry sliding wear behaviour of laser additive manufactured Ti-6Al-4V. Mater Today Proc 2018;5(1, Part 1):397–402. URL: http://www.sciencedirect.com/science/article/pii/S2214785317323350. doi:https://doi.org/10.1016/j.matpr.2017.11.097.

[23] Chandramohan, P., Bhero, S., Obadele, B.A., Olubambi, P.A.. Laser additive manufactured Ti–6Al–4V alloy: tribology and corrosion studies. Int J Adv Manuf Technol 2017;92(5):3051–3061. URL: https://doi.org/10.1007/s00170-017-0410-2. doi:10.1007/

s00170-017-0410-2.

[24] Philippon, S.. Etude expérimentale du frottement sec à grandes vitesses de glissement. Ph.D. thesis; Université de Metz; 2004. URL: https://www.theses.fr/2004METZ016S.

[25] Chassaing, G., Pougis, A., Philippon, S., Lipinski, P., Meriaux, J., Faure, L.. Initiation of Adhesive Wear During Frictional Interaction at Very High Velocity for a Ti6Al4V Tribopair. In: Proc. 13th World Conf. Titan. May. ISBN 9781119296126; 2016, p. 5–7. doi:10.1002/9781119296126.ch274.

[26] Khorasani, A., Gibson, I., Awan, U.S., Ghaderi, A.. The effect of SLM process parameters on density, hardness, tensile strength and surface quality of Ti-6Al-4V. Addit Manuf 2019;25:176–186. URL: http://www.sciencedirect.com/science/article/pii/S2214860418305670. doi:https://doi.org/10.1016/j.addma.2018.09.002.

[27] Xu, Y., Zhang, D., Guo, Y., Hu, S., Wu, X., Jiang, Y.. Microstructural tailoring of As-Selective Laser Melted Ti6Al4V alloy for high mechanical properties. J Alloys Compd 2020;816:152536. URL: http://www.sciencedirect.com/science/article/pii/S092583881933782X. doi:https://doi.org/10.1016/j.jallcom.2019.152536.

[28] Pitassi, D.. Finite Element Thermal Analysis of Metal Parts Additively Manufactured via Selective Laser Melting. Rijeka: IntechOpen. ISBN 978-953-51-3850-1; 2018, p. Ch. 6. URL: https://doi.org/10.5772/intechopen.71876. doi:10.5772/intechopen.71876.

[29] Barba, D., Alabort, C., Tang, Y.T., Viscasillas, M.J., Reed, R.C., Alabort, E.. On the size and orientation effect in additive manufactured Ti-6Al-4V. Mater Des 2020;186:108235. URL: http://www.sciencedirect.com/science/article/pii/S0264127519306732. doi:https://doi.org/10.1016/j.matdes.2019.108235.

[30] Guzanová, A., Ižaríková, G., Brezinová, J., Živčák, J., Draganovská, D., Hudák, R.. Influence of Build Orientation, Heat Treatment, and Laser Power on the Hardness of Ti6Al4V Manufactured Using the DMLS Process. 2017. doi:10.3390/met7080318.

[31] Mierzejewska, A.Ż., Hudák, R., Sidun, J.. Mechanical Properties and Microstructure of DMLS Ti6Al4V Alloy Dedicated to Biomedical Applications. 2019. doi:10.3390/ma12010176.

[32] Chassaing, G., Pougis, A., Philippon, S., Lipinski, P., Faure, L., Meriaux, J., et al. Experimental and numerical study of frictional heating during rapid interactions of a Ti6Al4V tribopair. Wear 2015;342:322–333. doi:10.1016/j.wear.2015.09.013.

[33] Adam, C., Jäger, C.. Simplified collapse capacity assessment of earthquake excited regular frame structures vulnerable to P-delta. Eng Struct 2012;44:159–173. URL: http://www.sciencedirect.com/science/article/pii/S0141029612002799. doi:https://doi.org/10.1016/j.engstruct.2012.05.036.

[34] Mohrbacher, H., Blanpain, B., Celis, J.P., Roos, J.R., Stals, L., Van Stappen, M.. Oxidational wear of TiN coatings on tool steel and nitrided tool steel in unlubricated fretting. Wear 1995;188(1):130–137. URL: http://www.sciencedirect.com/science/article/pii/0043164895066373. doi:https://doi.org/10.1016/0043-1648(95)06637-3.

[35] De Moerlooze, K., Al-Bender, F., Van Brussel, H.. A novel energy-based generic wear model at the asperity level. Wear 2011;270(11):760–770. URL: http://www.sciencedirect.com/science/article/pii/S0043164811000378. doi:https://doi.org/10.1016/j.wear.2011.01.028.

[36] Ramalho, A., Miranda, J.C.. The relationship between wear and dissipated energy in sliding systems. Wear 2006;260(4):361–367. URL: http://www.sciencedirect.com/science/article/pii/S0043164805002541. doi:https://doi.org/10.1016/j.wear.2005.02.121.

[37] Jahangiri, M., Hashempour, M., Razavizadeh, H., Rezaie, H.R.. A new method to investigate the sliding wear behaviour of materials based on energy dissipation: W–25wt%Cu composite. Wear 2012;274-275:175–182. URL: http://www.sciencedirect.com/science/article/pii/S0043164811005679. doi:https://doi.org/10.1016/j.wear.2011.08.023.

[38] Cave, A., Roslyakov, S., Iskander, M., Bless, S.. Design and Performance of a Laboratory Pneumatic Gun for Soil Ballistic Applications. Exp Tech 2016;40(2):541–553. URL: https://doi.org/10.1007/s40799-016-0055-3. doi:10.1007/s40799-016-0055-3.

[39] Zhang, X., Vu-Quoc, L.. Modeling the dependence of the coefficient of restitution on the impact velocity in elasto-plastic collisions. Int J Impact Eng 2002;27(3):317–341. URL: http://www.sciencedirect.com/science/article/pii/S0734743X01000525. doi:https://doi.org/10.1016/S0734-743X(01)00052-5.

[40] Hu, S., Guo, X.. A dissipative contact force model for impact analysis in multibody dynamics. Multibody Syst Dyn 2015;35(2):131–151. URL: https://doi.org/10.1007/s11044-015-9453-z. doi:10.1007/s11044-015-9453-z.